

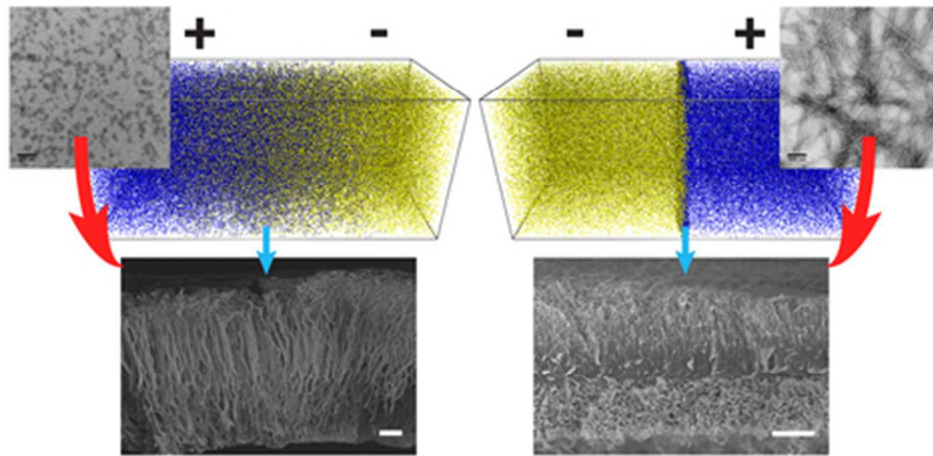


## Molecular Design for Growth of Supramolecular Membranes with Hierarchical Structure

Journal:	<i>Soft Matter</i>
Manuscript ID	SM-ART-09-2015-002381.R1
Article Type:	Paper
Date Submitted by the Author:	13-Nov-2015
Complete List of Authors:	Zha, R. Helen; Technische Universiteit Eindhoven, MST Velichko, Yury; Northwestern University, Bitton, Ronit; Ben-Gurion University of the Negev, Stupp, Samuel; Northwestern University,

Textual abstract for ToC graphic:

Computational and experimental investigation of interfacial self-assembly between peptide amphiphiles and polyelectrolytes into microstructured membranes.



39x19mm (300 x 300 DPI)



## Molecular Design for Growth of Supramolecular Membranes with Hierarchical Structure

R. Helen Zha,<sup>a</sup> Yuri S. Velichko,<sup>a</sup> Ronit Bitton,<sup>b</sup> Samuel I. Stupp<sup>a,b,c</sup>

Received 00th January 20xx,  
Accepted 00th January 20xx

DOI: 10.1039/x0xx00000x

[www.rsc.org/](http://www.rsc.org/)

Membranes with hierarchical structure exist in biological systems, and bio-inspired building blocks have been used to grow synthetic analogues in the laboratory through self-assembly. The formation of these synthetic membranes is initiated at the interface of two aqueous solutions, one containing cationic peptide amphiphiles (PA) and the other containing the anionic biopolymer hyaluronic acid (HA). The membrane growth process starts within milliseconds of interface formation and continues over much longer timescales to generate robust membranes with supramolecular PA-HA nanofibers oriented orthogonal to the interface. Computer simulation indicates that formation of these hierarchically structured membranes requires strong interactions between molecular components at early time points in order to generate a diffusion barrier between both solutions. Experimental studies using structurally designed PAs confirm simulation results by showing that only PAs with high zeta potential are able to yield hierarchically structured membranes. Furthermore, the chemical structure of such PAs must incorporate residues that form  $\beta$ -sheets, which facilitates self-assembly of long nanofibers. In contrast, PAs that form low aspect ratio nanostructures interact weakly with HA and yield membranes that exhibit non-fibrous fingering protrusions. Furthermore, experimental results show that increasing HA molecular weight decreases the growth rate of orthogonal nanofibers. This result is supported by simulation results suggesting that the thickness of the interfacial contact layer generated immediately after initiation of self-assembly increases with polymer molecular weight.

### Introduction

Strategies to achieve hierarchical self-assembly in soft matter is an important bio-inspired scientific goal since it is a great source of function. Hierarchical structures in supramolecular systems arise from non-covalent organization of the building blocks across multiple length scales, with the potential to yield functional materials [1,2]. Small changes in molecular structure of the building blocks can lead to large changes in hierarchical structure [3,4]. Because hierarchical self-assembly is bio-inspired, the use of basic biological building blocks such as peptides, nucleic acids, fatty acids, and polysaccharides is a valuable strategy to develop the underlying science. Peptide amphiphiles (PAs) have shown great promise and versatility as a platform for biomimetic bioactive materials [5-9]. PAs consisting of a hydrophobic region, typically an alkyl tail, and a hydrophilic peptide sequence have been shown to aggregate in water to form nanoscale structures. Additionally, PAs that

incorporate a  $\beta$ -sheet forming region are capable of forming one-dimensional high aspect ratio nanostructures such as cylindrical nanofibers [5], ribbons [10,11], and twisted helices [12] due to the stabilizing effects of hydrogen bonding along the long axis [13-16].

PA nanostructures can display on their surfaces charged amino acids capable of engaging in strong electrostatic interactions; they may additionally assemble in water under certain conditions into hierarchical materials such as monodomain aligned gels [17] and repulsion-mediated crystalline domains [18]. Self-assembly of PA nanostructures with biopolymer polyelectrolytes into hierarchically ordered membranes has also been observed [19-24]. Stupp and co-workers reported the rapid formation of a robust membrane at the interface between an aqueous solution of a cationic PA and an aqueous solution of hyaluronic acid (HA), an anionic charged glycosaminoglycan. Membrane self-assembly is initiated by the rapid complexation of PA and HA to form a diffusion barrier between the two solutions. Furthermore, excess osmotic pressure promotes reptation of HA molecules through the diffusion barrier and into the PA solution, templating the growth of nanofiber bundles aligned orthogonal to the interface [19]. The membrane formation process begins within milliseconds after interface formation and can continue for hours to days depending on availability of molecules in solution.

<sup>a</sup> Department of Materials Science and Engineering, Northwestern University, 2220 Campus Drive, Evanston, IL 60208, USA

<sup>b</sup> Simpson Querrey Institute for BioNanotechnology, Northwestern University, 303 East Superior Street, 11th floor, Chicago, IL 60611, USA

<sup>c</sup> Departments of Chemistry, Medicine, and Biomedical Engineering, Northwestern University, 2220 Campus Drive, Evanston, IL 60208, USA.

Electronic Supplementary Information (ESI) available: SAXS fittings, additional SEM microscopy images, and  $\zeta$ -potential and osmolality measurements of HA. See DOI: 10.1039/x0xx00000x

Previous work has demonstrated the possibility of directing orthogonal nanofiber growth using electric fields [20] as well as the influence of solution concentration and osmotic pressure on membrane structure and properties [21]. Studies have also suggested that strong PA-polyelectrolyte interaction and the presence of high aspect ratio PA nanofibers in solution facilitate diffusion barrier formation and orthogonal nanofiber growth [22–24]. Differences in membrane structure that result from variation of such factors in the self-assembly process can have dramatic consequences on membrane function. For example, membranes assembled from anti-cancer PAs bearing the (KLAKLAK)<sub>2</sub> epitope exhibit orthogonal nanofiber structure if sufficient PA nanofibers are present in solution prior to interfacial self-assembly. These nanofibrous membranes only display cytotoxicity towards cancer cells in direct contact with the membrane surface. However, insufficient presence of PA nanofibers results in formation of non-fibrous membranes that can slowly release cytotoxic (KLAKLAK)<sub>2</sub> components into surrounding media [23]. Thus, understanding the key factors in membrane self-assembly is important in rational control over membrane design and application. It is evident that interfacial aggregation at early times are crucial aspects of membrane formation, but such millisecond time points are difficult to observe experimentally. Therefore, we have performed here computer simulations to explore the processes that occur immediately after initiation of membrane self-assembly. Guided by simulation results, we experimentally investigate the effect of systematic changes to supramolecular building blocks on the structure and properties of our peptide amphiphile-polymer membranes.

## Results and Discussion

Membrane formation between PA molecules and oppositely charged polyelectrolytes such as HA is a hierarchical self-assembly process across multiple time and length scales. PA molecules form nanostructures in aqueous solution and further assemble with HA upon contact into macroscopic membranes exhibiting evolving microstructure. We simulate this system using two boundary condition compartments and one central reaction compartment (Figure 1A). The interfacial charge-charge aggregation process can be characterized by measuring the width and the density of the contact layer, which is determined by the spatial distribution of non-aggregated (i.e. HA polymer and PA nanostructures) and aggregated (i.e. complexed PA-HA) components. Figure 1B shows a snapshot of the computational model. Figure 1C shows a density profile for each component and the whole system, where the densities  $\rho_A$ ,  $\rho_B$ , and  $\rho_{A+B}$  are calculated by dividing the system volume into bins along the Y direction and averaging the number of components in each bin. It should be noted here that the densities take into account both non-aggregated and aggregated species. Such analysis allows us to examine diffusion and aggregation of components simultaneously.

Our molecular simulations predict significant structural changes in the interfacial contact layer formed immediately

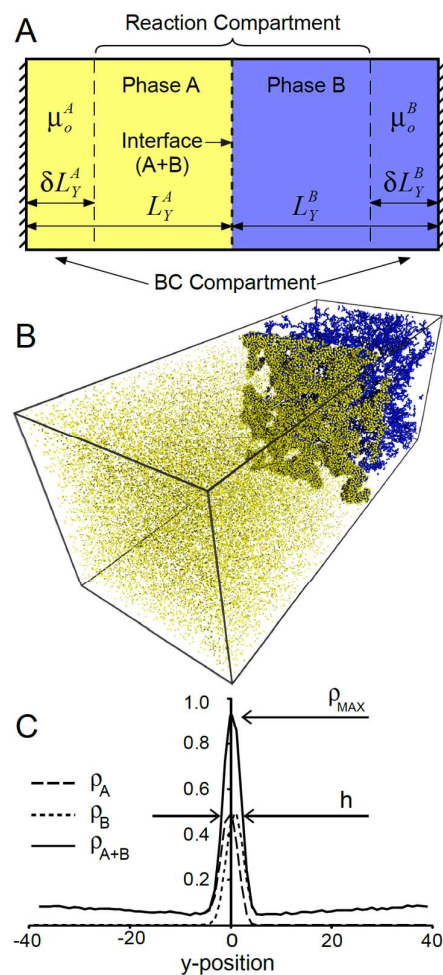


**Fig. 1** (A) Schematic representation of a computational model with two components interacting at the interface. (B) Snapshot of the membrane formed at the interface between two solutions consisting of A-monomers ( $N_A=1$ ) and B-chains ( $N_B=64$ ) at  $r_0=0.05s^{-3}$  and  $\epsilon_{AB}=8k_B T$ . (C) Density profile for each component and the whole system.

after initiation of self-assembly. These changes depend on strength of the interaction between PA nanostructures and HA chains. Figures 2A and 2B show snapshots of the system in cases of strong and weak interactions between PA and HA components. In the case of weak interaction energies, where  $\epsilon_{AB} \leq 4$ , the contact layer consists of small PA-HA aggregates resulting from charge complexation. This contact layer broadens with time, as the width appears to be time-dependent (Figure 2D). The density within the contact layer stabilizes at small values, suggesting a dynamic equilibrium between non-aggregated components and small aggregates. On the other hand, in the case of strong interaction energies, where  $\epsilon_{AB} > 6$ , influx and strong intermolecular forces support continuous aggregation of unaggregated components and small clusters until they percolate, giving a compact contact layer. This process slows down the diffusion of non-aggregated components and shrinks pores in the contact layer, effectively establishing a dense barrier to diffusion (Figure 2C).

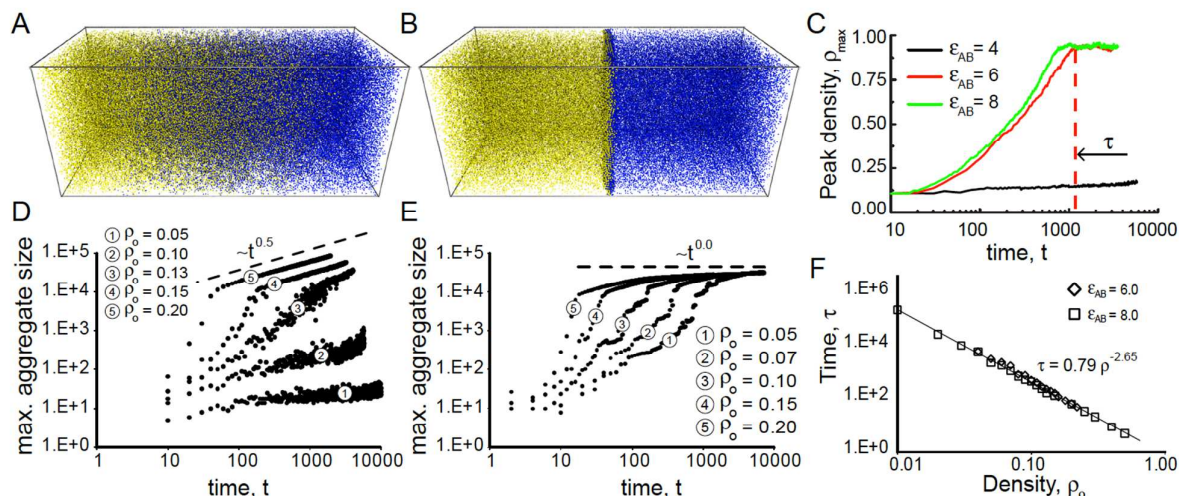
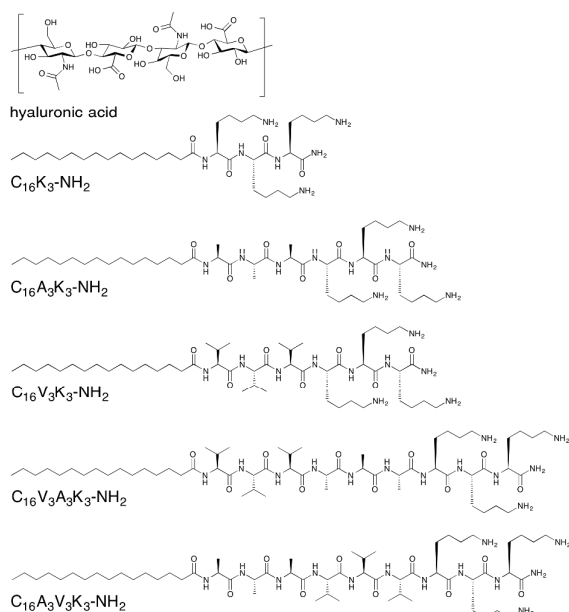


**Fig. 2** Snapshots of two systems in the case of weak (A)  $\epsilon_{AB}=4k_B T$  and strong (B)  $\epsilon_{AB}=8k_B T$  intermolecular interactions. (C) Peak density vs. time for different values of  $\epsilon_{AB}$ . Time of the contact layer formation,  $t$ , is determined at the moment when density plateaus. Largest aggregate size vs. time for different densities in the case of (D) weak  $\epsilon_{AB}=4k_B T$  and (E) strong  $\epsilon_{AB}=8k_B T$  intermolecular interactions. (F) Time to diffusion barrier formation as a function of initial density.

Many interesting details about contact layer formation important to understanding the aggregation mechanism at early time steps vanish during the density calculations as a result of averaging. For example, a size distribution of the aggregates and evolution of its elements with time would provide an almost complete description of the whole aggregation process. On the other hand, such detailed analysis is complicated and computationally expensive. We find that tracking the growth of the largest aggregate at the interface is informative enough, since the largest aggregate can essentially be considered to be the contact layer. Figures 2D and 2E show size of the largest aggregate as a function of time for systems

with different bulk densities and interaction energies. In the limit of strong interactions (Figure 2E) the size of the largest aggregate approaches a constant value over time, indicating that the contact layer ceases to increase in thickness due to establishment of a diffusion barrier. The time to diffusion barrier formation scales linearly with initial density (Figure 2F). However, in the limit of weak interactions (Figure 2D), the nature of the interfacial aggregation is fundamentally different, as the size of the largest aggregate continues to increase with  $t^{0.5}$ , which is consistent with predictions of the one dimensional model [25,26].

The simulations carried out here capture the importance of intermolecular interactions among the supramolecular and polymeric components. Therefore, to experimentally explore these interactions, we synthesized a set of PAs capable of forming nanostructures that vary in intermolecular interaction strength. PAs bearing identical cationic headgroups but different self-assembly domains were synthesized (Scheme 1). These PAs systematically include or exclude valine residues, which promote  $\beta$ -sheet formation [27,28], as well as alanine residues, which act as a neutral linker. Circular dichroism (CD) shows that  $C_{16}K_3$  and  $C_{16}A_3K_3$ , which lack residues with high  $\beta$ -sheet propensity, reveal primarily a signal associated with random peptide coils.  $C_{16}V_3K_3$  and  $C_{16}V_3A_3K_3$ , which incorporate valine residues immediately adjacent to the hydrophobic tail, show a mixture of  $\beta$ -sheet and random coil CD signal (Figure 3A). Interestingly,  $C_{16}A_3V_3K_3$  exhibits predominantly  $\beta$ -sheet signal, suggesting that positioning alanine residues immediately adjacent to the hydrophobic tail can allow them to act as flexible linkers and improve hydrogen bond packing within the nanostructure. Such drastic sequence-dependent changes are not surprising, as previous research has shown that in the case of cylindrical nanofibers, the extent of  $\beta$ -sheet formation parallel to the long axis significantly affects nanofiber properties as well as hydrogel networks



**Scheme 1** Chemical structures of hyaluronic acid and cationic PAs synthesized.

created by nanofibers after charge screening. Specifically, it was shown that such effects result merely from rearrangement or substitution of valine and alanine residues adjacent to the hydrophobic tail [16].

Conventional TEM and SAXS were used to further probe the nanostructure formation of PAs in water (Figure 4). Both techniques suggest that  $C_{16}K_3$  and  $C_{16}A_3K_3$  exhibit spherical morphology and that the nanostructures themselves aggregate in solution (Figures 4B and 4E), particularly in the case of  $C_{16}A_3K_3$ . Specifically, the SAXS profiles of these PAs show slope of 0 at low  $q$ , indicating spherical morphology, but also show a significant structure factor, indicating large-scale short-range ordering [29] (Figure 4F). These morphological results correlate well with CD data, as self-assembly of high aspect ratio structures is not expected without  $\beta$ -sheet formation. In contrast, high aspect ratio nanofibers are the primary structures observed in PAs with valine residues positioned between the hydrocarbon tail and charged headgroup.  $C_{16}V_3K_3$  consists almost entirely of long nanofibers (Figure 4A), while inclusion of alanine residues in the peptide sequence (i.e.  $C_{16}V_3A_3K_3$  and  $C_{16}A_3V_3K_3$ ) leads to the appearance of some shorter nanofibers (Figures 4C and 4D). The SAXS profiles of PAs were fitted to polydisperse cylindrical and spherical core-shell models (Figure S1). Furthermore, osmolality measurements show that nanofiber-forming PAs have much lower osmotic pressures in solution than micelle-forming PAs due to the increased number of large structures in solution at similar concentrations by weight (Figure 3B). However, osmolality difference between PA solutions is not expected to play a significant role in membrane formation, as the absorption of counterions by HA from the PA solution upon contact dominates the establishment of osmotic pressure across the interface [21].

In our investigation, all PA molecules contain the same formal charge. However,  $\zeta$ -potential measurements (Figure 3C) show the differences in surface charge density among PA nanostructures resulting from geometric and molecular packing considerations. PA molecules within spherical aggregates are not as closely packed as those within cylindrical nanofibers, as previous research shows that greater  $\beta$ -sheet character leads to more solid-like dynamics in amino acids adjacent to the hydrophobic core of a nanofiber [30]. Therefore, the trend in PA  $\zeta$ -potentials is consistent with our characterization of their secondary structure and nano-morphology described earlier. Importantly, these  $\zeta$ -potential values experimentally represent the interaction energy parameter in our simulations and inherently incorporate nanostructure shape, which our simulations do not consider. It is worthwhile to note that the pH (at 1 wt% in MilliQ water) of all PAs used in our studies fall within a narrow range between 6.4-7. Previous studies have shown that  $C_{16}V_3A_3K_3$  PA has an isoelectric point of pH 10.3 and that  $\zeta$ -potential does not change appreciably between pH 5-9 [31]. Furthermore, the pH of all HA solutions used fall between 6-7, and studies have demonstrated that hierarchically assembled PA structures also do not vary between pH 5-9 [19,31]. Therefore, the differences seen among our PA molecules can be attributed to their

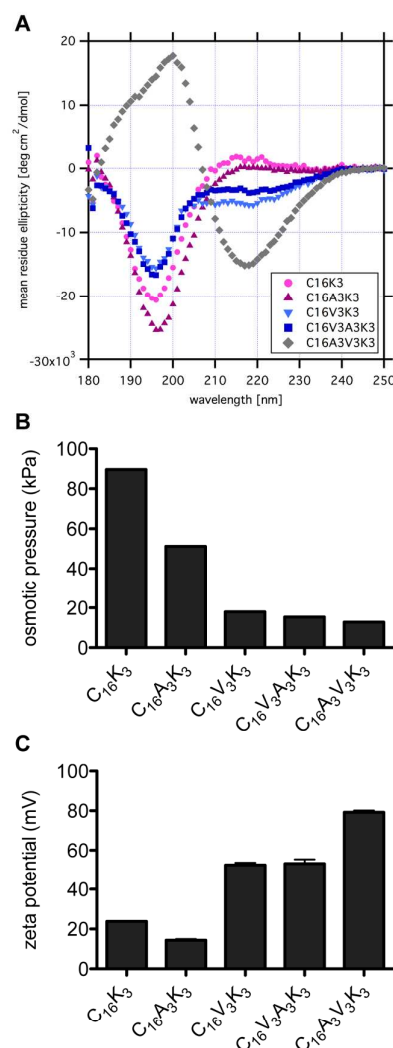


**Fig. 3** (A) Circular dichroism of PAs at 0.1 mg/mL in water. (B) Osmotic pressure of PAs at 10 mg/mL in water. (C) Zeta potential of PAs at 1 mg/mL.

inherent self-assembly behavior rather than to slight variations in solution pH.

Our molecular simulations suggest that the mechanism of membrane self-assembly can be categorized into regimes of strong or weak interaction strength between components, and that membrane microstructure should differ in these two regimes. Indeed, membranes assembled from the nanofiber-forming PAs  $C_{16}V_3K_3$  and  $C_{16}V_3A_3K_3$  exhibit morphological features predicted by simulation. Within minutes after initiation of self-assembly, these membranes show a thin, dense interfacial contact layer (Figure S2). After 30 minutes of self-assembly, PA-HA nanofibers templated by the slow reptation of HA chains perpendicular to the contact layer are observed (Figures 5A and 5D). These membranes are robust and optically clear, further indicating the establishment of a diffusion barrier at the interface. In contrast, membranes formed with the spherically aggregated PAs,  $C_{16}K_3$  and  $C_{16}A_3K_3$ , are not robust and are more opaque within minutes after

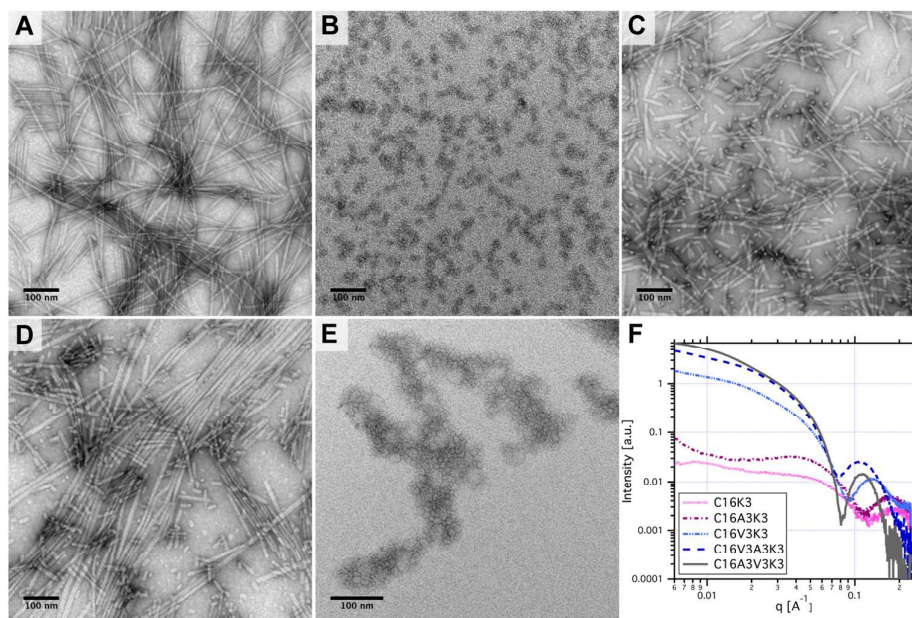


**Fig. 4** Conventional TEM imaging of (A)  $C_{16}V_3K_3$ , (B)  $C_{16}K_3$ , (C)  $C_{16}A_3V_3K_3$ , (D)  $C_{16}V_3A_3K_3$ , and (E)  $C_{16}A_3K_3$ . (F) SAXS of PA nanostructures in water at 10 mg/mL.

contact between the PA and HA solutions. SEM shows that these membranes are much thicker and have an altered morphology with no obvious diffusion barrier or nanofiber growth orthogonal to the contact layer (Figures 5B and 5E). Finger-like branches extending from the PA compartment into the HA compartment are seen (Figure 5F). These fingers lack fibrous texture and are likely comprised of aggregated HA and PA formed by unhindered diffusion of PA nanostructures into the HA compartment. The fingering morphology is further indicative of directional diffusion-limited aggregation from a planar source [32,33].

The two distinct types of membrane structure discussed

above correlate well with our  $\zeta$ -potential measurements and simulation results. Assembly of HA with high  $\zeta$ -potential PA nanofibers results in a robust membrane consisting of a rapidly formed diffusion barrier and growing PA-HA nanofiber orthogonal to the interface, while assembly of HA with low  $\zeta$ -potential PA nanospheres results in weak non-fibrous membranes with long finger-like structures consisting of aggregated HA and PA. In the case of  $C_{16}A_3V_3K_3$ , we expect a strong interaction with HA chains as a result of charge density and in fact we do observe formation of a contact layer (Figure 5C). However, the high  $\beta$ -sheet character of this PA leads to extremely high surface charge density, which evidently yields a

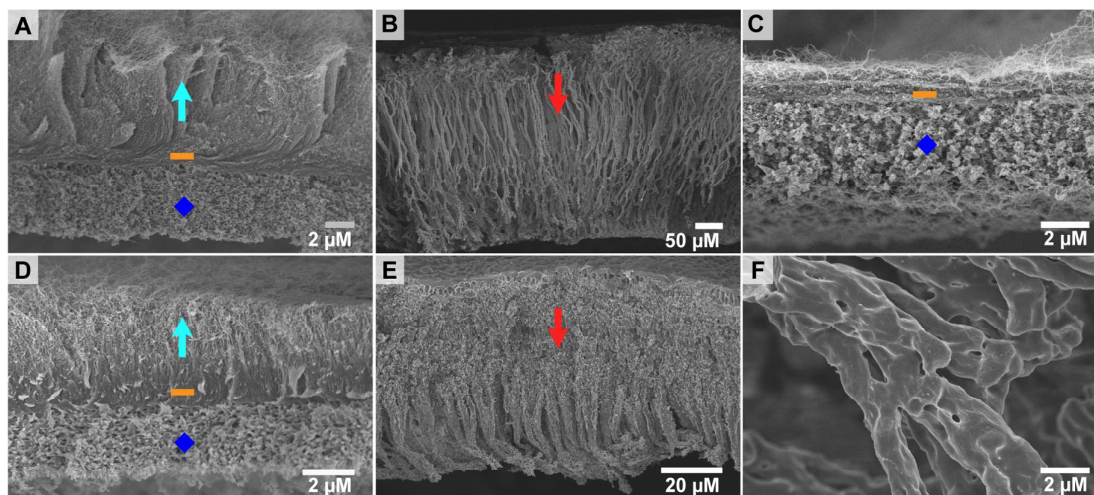


**Fig. 5** SEM microscopy of membranes fabricated from self-assembly of HA with (A)  $C_{16}V_3K_3$ , (B)  $C_{16}K_3$ , (C)  $C_{16}A_3V_3K_3$ , (D)  $C_{16}V_3A_3K_3$ , and (E)  $C_{16}A_3K_3$ . The top and bottom of each image corresponds to the PA and HA compartment, respectively. Diffusion barriers are indicated by orange lines, orthogonal PA/HA nanofiber bundles are indicated with a blue arrow in the direction of HA chain reptation, and regions of amorphous HA associated with the membrane are indicated with blue diamonds. In images showing thick non-fibrous membranes, the direction of PA diffusion and finger formation is indicated by a red arrow. (F) Close-up of finger structures seen for  $C_{16}K_3$ .

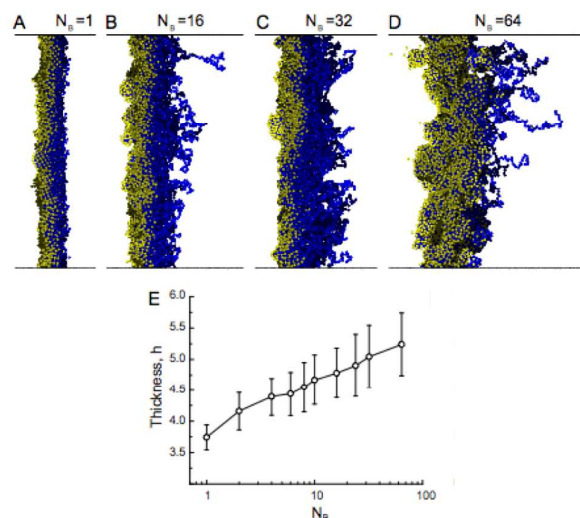


**Fig. 6** Snapshots of the contact layers formed in the case of strong ( $\epsilon_{AB}=8k_B T$ ) intermolecular interactions from A-monomers ( $N_A=1$ ) and B-chains consisting of (A)  $N_B=1$ , (B)  $N_B=16$ , (C)  $N_B=32$  and (D)  $N_B=64$  units. (E) Thickness of the contact layer,  $h$ , as a function of the B-chains length,  $N_B$ .

contact layer so dense that no orthogonal nanofiber growth is found. This result suggests that these strong interfacial interactions cause HA chains and  $C_{16}A_3V_3K_3$  nanostructures to continue to aggregate within the contact layer for a long time after structures that percolate the contact layer form. This could in turn result in extreme densification of the diffusion barrier, preventing even the slow outward reptation of HA over the timescale of the experiment.

We have thus far shown that changes in the PA chemical structure can cause large differences in membrane microstructure and properties. Simulations also suggest that systematic variation of HA molecular weight can result in dramatic changes as well. When PA and HA solutions are brought into the contact, components diffuse toward each

other and start to interact at the interface. In a simulation scenario where both components are identical in size, the initial width of the contact layer can be approximated by the diffusion length,  $l_D = s(D_o\rho_0t/\rho)^{0.5}$ , where  $D_o$  is a diffusion coefficient at a given concentration  $\rho_0$  [34]. However, change in the molecular length of the polymer component (i.e. component B) breaks the symmetry of the system, since the diffusion coefficient depends on the polymer length and concentration [35,36]. Polymer solutions can be characterized by the radius of gyration of the chain,  $R_G[B]$ . In the case of very long polymers, we can consider them as a static component with density fluctuations varying on the scale of  $R_G[B]$ . Taking into account the inverse relationship of  $R_G[B]$  and  $l_D[B]$ , we could expect different behavior in short and long polymer chains. In the case of short polymers,  $l_D[A] \gg R_G[B]$ , and we imagine interpenetrating fronts of both HA and PA components forming the contact layer as a result of molecular aggregation at the initial interface. In the case of long polymers,  $l_D[A] \ll R_G[B]$  and only a single front of diffusing PA continuously penetrates and condenses a network of static, entangled polymers. In this scenario, the structure of the contact layer is significantly affected by the structure of the polymer solution at the interface. Figures 6A-D show snapshots from simulations of the contact layer formed from the A component ( $N_A=1$ ) and B-chains ( $N_B=1, 16, 32$  and  $64$ ) in the limit of strong interactions. An important result is that the thickness of the contact layer increases with the chain length (Figure 6E).

To complement simulation results, we investigated experimentally the effect of polymer molecular weight on membrane formation. For all HA molecular weights used, the concentration by mass is kept constant, thus conserving the total number of charges in solution. Moreover, no trends in osmotic pressure are seen among the different molecular weights (Figure S3A), and all HA molecular weights exhibit high  $\zeta$ -potential (Figure S3B). As simulations predicted, we found that membranes formed by different molecular weight HA vary

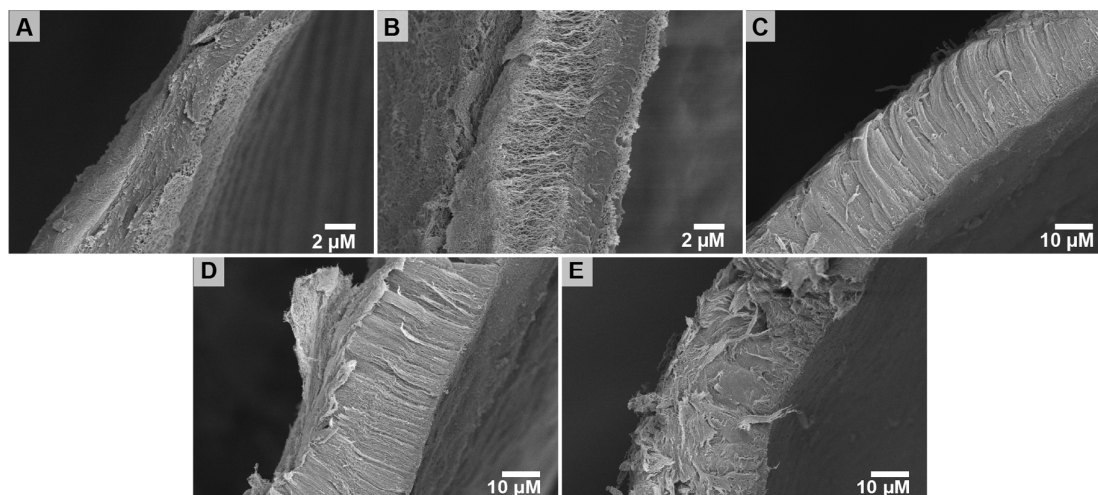


**Fig. 7** SEM microscopy of membranes fabricated from self-assembly of  $C_{16}V_3A_3K_3$  with (A) 2 MDa, (B) 1.7 MDa, (C) 910kDa, (D) 741kDa, and (E) 357kDa. The left and right of each image corresponds to the PA and HA compartments, respectively.

in structure. SEM indicates that although all membranes exhibit a diffusion barrier indicative of high interaction strength, membranes formed with the highest HA molecular weight (2 MDa) do not show perpendicular nanofiber growth even after 3 hr of contact between PA and HA solutions. Membranes formed with lower molecular weights exhibit increasing growth rates of fibrous material orthogonal to the membrane plane and thus the thickness of the orthogonal nanofiber region increases as molecular weight decreases (Figure 7). This trend in the growth rate of orthogonal nanofibers is likely due to the decreased thickness of contact layers created by shorter chains. Similarly, the lack of orthogonal nanofibers in membranes formed with 2 MDa HA likely results from a thick contact layer formed by long, entangled chains. Alignment of the orthogonal nanofiber region also seems to decrease with decreasing molecular weight, possibly due to the shorter end-to-end length of lower molecular weight chains.

## Experimental

### Peptide Synthesis

PAs (Scheme 1) were synthesized using standard fluorenylmethoxycarbonyl (Fmoc) solid-phase peptide synthesis on rink amide resin and purified using reversed-phase high-performance liquid chromatography in an acidic acetonitrile/water gradient containing 0.1% trifluoroacetic acid. After lyophilization of purified PAs, residual trifluoroacetic acid counterions were exchanged by sublimation from 1 mg/mL PA solution in 0.01 M HCl. PAs were then resolubilized in ultrapure 18.2 MW-cm Milli-Q water (Millipore), lyophilized, and stored at -20 °C for no longer than 6 months until used for experiments.

### Transmission Electron Microscopy

Samples for transmission electron microscopy (TEM) were prepared by dissolving PAs at 2.5 mg/mL and placing 10  $\mu$ L solution onto a 300 mesh copper grid with an amorphous carbon support film (Electron Microscopy Sciences). The solution was wicked after 2 min and allowed to dry for 10 min before staining with 2% uranyl acetate. Imaging was performed on a JEOL 1230 TEM with a Hamamatsu ORCA camera at an accelerating voltage of 100 kV.

### Small Angle X-Ray Scattering

Small angle x-ray scattering (SAXS) measurements were performed using beam line 5ID-D in the DuPont-Northwestern-Dow Collaborative Access team (DND-CAT) Synchrotron Research Center at the Advanced Photon Source, Argonne National Laboratory. Energy of 15 keV was selected using a double-crystal monochromator, and data was collected using a CCD detector (MAR) positioned 245 cm behind the sample. The scattering intensity was recorded in the interval  $0.008 < q < 0.25 \text{ \AA}^{-1}$ . The wave vector defined as  $q = (4\pi/\lambda) \sin(\theta/2)$ , where  $\theta$  is the scattering angle. PA solution samples were placed in 1.5 mm quartz capillaries and were exposed to x-rays for 4–8 s,

depending on scattering intensity. The 2-D SAXS images were azimuthally averaged to produce one-dimensional profiles of intensity using the two-dimensional data reduction program FIT2D. The scattering of the sample holder with water was also collected and subtracted from the corresponding data.

### Scanning Electron Microscopy

Membranes were formed using 10 mg/mL PA and 10 mg/mL HA aqueous solutions. PAs were synthesized as described above and dissolved in MilliQ water for at least 1 h prior to use. Research grade or higher sodium hyaluronate powders with molecular weights of 2 MDa, 1.7 MDa, 910 kDa, 741 kDa, 357 kDa, and 234 kDa were purchased from Lifecore Biomedical, Inc and were dissolved in MilliQ water overnight before use. Planar sheet membranes were formed inside circular polyurethane washers (0.2 in inner diameter, McMaster-Carr) by layering 50  $\mu$ L PA solution on top of 50  $\mu$ L HA solution. Membranes were allowed to incubate at room temperature for 3 h prior to washing with MilliQ water.

Scanning electron microscopy (SEM) was used to image the cross-section of planar membranes, which were fabricated as described in the previous section. After washing both sides with MilliQ water, samples were fixed in 2% glutaraldehyde with 3% sucrose overnight at room temperature prior to dehydration using a stepwise gradient of 20% to 100% ethanol in water. In order to preserve the hydrated structure of samples, critical point drying was performed with a Tousimis SAMDRI-795 critical point dryer. Dried samples were manually torn to expose the cross-section and were mounted to SEM stubs using carbon tape. Finally, samples were coated with 8 nm of osmium using an osmium plasma coater (Structure Probe, Inc.) and imaged by a LEO 1525 field emission SEM using an accelerating voltage of 3 kV.

### $\zeta$ -Potential Measurement

PA or HA was dissolved in MilliQ water at a concentration of 1 mg/mL and loaded into folded capillary cells (Malvern Instruments).  $\zeta$ -potential measurements were performed at 25 °C using a Zetasizer Nano ZS (Malvern Instruments). For each PA or HA, 3 separate samples were measured and at least 5 runs were made per sample.

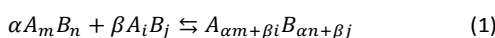
### Circular Dichroism

The secondary structure and  $\beta$ -sheet formation of PAs was probed using circular dichroism (CD) at 22 °C. PAs were dissolved in MilliQ water at a concentration of 0.1 mg/mL and measured with a JASCO J-715 CD spectrophotometer in a 1 mm pathlength quartz cuvette. From the data, mean residue ellipticity was calculated by assuming 90% peptide content.

## Modeling and Simulation

To understand the mechanism of membrane formation, in particular the aggregation of components immediately after initiation of self-assembly to form a contact layer, we developed a corresponding reaction-diffusion model and carried out a coarse-grained molecular dynamics simulation.

Here we consider a system of two solutions initially separated by the interface and each composed of components of only one kind, A or B. Upon contact of the two solutions, their components create a reaction-diffusion field and the dynamic balance between directional diffusion and aggregation of interpenetrating fronts determines the distinctive course of the interfacial self-assembly. We assume that both components interact locally through non-covalent forces and undergo reversible association reactions through the adsorption and emission of small aggregates or free species. For example, PA molecules tend to aggregate in aqueous solution and the interaction between single PA molecules or different PA aggregates with long HA chains should be considered separately due to possibility of structural changes that could be induced by PA-HA interactions, which can be summarized as a system of equations,



where the stoichiometric coefficients  $\alpha$ ,  $\beta$ ,  $m$ , and  $n$  are positive integer numbers. Chemical equilibrium in the system is established as a result of diffusion of aggregated and non-aggregated species as well as association and dissociation reactions that can be summarized by a system of reaction-diffusion equations,

$$\frac{d}{dt} \rho_{mn} = D_{mn} \Delta \rho_{mn} + J_{mn} \quad (2)$$

where  $\rho_{mn}$  is the density of the  $A_m B_n$  aggregates,  $D_{mn}$  is the diffusion coefficient, and  $J_{mn}$  is the flux of aggregates that describes the association and disassociation reactions (Equation 1) affecting the concentration of  $A_m B_n$  aggregates. For the sake of simplicity, we studied systems assuming initial aggregate-free solution structure, i.e. the density of aggregates  $\rho_{mn}(t=0) = \rho[A_m B_n](t=0) = 0$  for all non-zero pairs of  $m$  and  $n$ . Thus, the corresponding initial conditions (ICs) are:

$$\rho[A](y, t=0) = \rho_A^0 H(-y) \quad (3.1)$$

$$\rho[B](y, t=0) = \rho_B^0 H(y) \quad (3.2)$$

and the boundary conditions (BCs) are:

$$\rho[A](-\infty, t) = \rho_A^0 \quad (4.1)$$

$$\rho[A](\infty, t) = 0 \quad (4.2)$$

$$\rho[B](-\infty, t) = 0 \quad (4.3)$$

$$\rho[B](\infty, t) = \rho_B^0 \quad (4.4)$$

where  $H(y)$  is the Heaviside unit step function,  $\rho[A](y, t)$  and  $\rho[B](y, t)$  are the densities of free A and B components at the position  $y$  and time  $t$ . The density of the aggregates and the aggregate size distribution are both key parameters to characterize interfacial self-assembly. In our study, we

analyzed both as a function of time and strength of intermolecular interactions.

The simulation was performed in a rectangular box with dimensions of  $L_X \times L_Y \times L_Z$ , where the original interface is parallel to the XZ-plane and is located in the center of the box along Y-direction. In order to introduce boundary conditions corresponding to Equations 3 and 4, we carried out a dual control volume grand canonical molecular dynamic simulation. Periodic boundary conditions were applied only in the X and Z directions. To incorporate proper boundary conditions for the Y-direction, the simulation system consists of three interacting compartments (Figure 1A): one at the center (C-compartment) and two on both sides (BC-compartment) along the Y-direction. Each BC-compartment is in direct contact with the C-compartment on a side that does not restrict molecular movement. On the other hand, the opposite boundary is considered as a hard wall. Thus, each BC-compartment can exchange free species with C-compartment so that constant densities of non-aggregated components at the corresponding boundaries of the C-compartment along the Y-direction can be fulfilled. The dimensions of the whole simulation box were chosen as  $L_X = L_Z = 80\sigma$  and  $L_Y = L_Y^A + L_Y^B$  where  $L_Y^A = L_Y^B = 100\sigma$ . To avoid significant density fluctuations in BC-compartments, the length along the Y-direction was chosen to be equal:  $\delta L_Y = \delta L_Y^A = \delta L_Y^B = 20\sigma$ .

A simulation was carried out within the framework of mixed Monte Carlo and stochastic dynamics. The stochastic dynamics simulation is performed in Cartesian space by solving Langevin's equations using the Langevin dynamics velocity Verlet method,

$$m_i \frac{d^2 \vec{r}_i}{dt^2} = -\frac{\partial U(\vec{r}_i, t)}{\partial \vec{r}_i} - \gamma m_i \frac{d\vec{r}_i}{dt} + \vec{\Gamma}_i(t) \quad (5)$$

where  $m_i$  is the mass and  $\vec{r}_i$  is the position vector of the  $i$ th particle,  $U(\vec{r}_i, t)$  is the total potential affecting the particle,  $\gamma = 1$  is the friction coefficient (damping constant in reciprocal time units), and  $\vec{\Gamma}_i(t)$  is a stochastic force satisfying the conditions of Gaussian white noise:

$$\langle \vec{\Gamma}_i(t) \vec{\Gamma}_i(t') \rangle = 2\gamma m_i k_B T \delta(t - t') \quad (6)$$

where  $k_B$  is the Boltzmann's constant,  $T$  is the temperature, and  $\delta(\cdot)$  is the delta function. The interactions between A and B particles is modeled with a short range Morse potential:

$$U_{AB}(r_{ij}) = \varepsilon_{AB} \left( \exp \left[ -2\alpha \frac{r_{ij} - \sigma}{\sigma} \right] - \exp \left[ -\alpha \frac{r_{ij} - \sigma}{\sigma} \right] \right) \quad (7)$$

where  $\varepsilon_{AB}$  determines the strength of interactions in  $k_B T$  units and  $r_{ij} = |\vec{r}_i - \vec{r}_j|$ . The interactions between identical particles were modeled with a first term that describes excluded volume interactions; e.g. for A-A pair:

$$U_{AA}(r_{ij}) = \varepsilon_{AA} \exp \left[ -2\alpha \frac{r_{ij} - \sigma}{\sigma} \right] \quad (8)$$

The constant  $\alpha = 24$  determines the shape of the potential and how fast it goes to zero. Each component is described as a polymer chain of length,  $N$ , that was varied from 1 to 128. For

connected “monomer” units, to maintain the distance between monomers and to prevent chains from crossing each other, a finite extendable non-linear elastic (FENE) potential [37] is used:

$$U_F(l_i) = \frac{l_0^2 k_F}{2} \ln \left[ 1 - \left( \frac{l_i}{l_0} \right)^2 \right] \quad (9)$$

where  $l_i = |\vec{r}_i - \vec{r}_j|$  is the bond length and  $k_F = 50 \varepsilon_{AB} / \sigma^2$  is the spring constant. The FENE potential is harmonic at its minimum, but the bonds cannot be stretched beyond  $l_0 = 1.5\sigma$ . We studied a number of systems with the free component density,  $\rho_A^0$  and  $\rho_B^0$ , varying in the range of  $0.01\sigma^{-3}$  to  $0.03\sigma^{-3}$  and the interaction energy  $\varepsilon_{AB}$  varying in the range of  $4k_B T$  to  $8k_B T$ .

To maintain a constant chemical potential in each boundary compartment, a Monte Carlo step was performed after each stochastic dynamics step and included the creation or removal of randomly selected particles in BC-compartments. An attempt to create a new particle depends on the present density of the system [38,39] and, therefore, corresponding correction factors were included in the calculation of the Boltzmann factor:

$$\exp \left( \frac{\mu_0^i - \Delta E}{k_B T} + N_i \ln \left( \frac{V_i}{\Lambda^3} \right) \right) \geq R \quad (10)$$

where  $N_i$  is the number of particles of component  $i$  in each BC-compartment,  $V_i$  is the volume of each BC-compartment,  $\mu_0^i$  is the desired chemical potential of component  $i$ ,  $\Delta E$  is the energy change due to creating or removing a particle, and  $R$  is a random number from (0,1).  $\Lambda$  is the thermal de Broglie wavelength, which determines the average interparticle spacing in classical gasses and liquids. Thus, the probability of creating or removing a new particle is given by:

$$\Pi_i^+ = \min \left\{ 1, \frac{Z_i V_i}{N_i + 1} \exp \left( \frac{\Delta E}{k_B T} \right) \right\} \quad (11.1)$$

$$\Pi_i^- = \min \left\{ 1, \frac{N_i}{Z_i V_i} \exp \left( \frac{\Delta E}{k_B T} \right) \right\} \quad (11.2)$$

where  $Z_i = \Lambda^{-3} \exp(\mu_0^i / k_B T)$  is the absolute activity.

## Conclusions

We have investigated the hierarchical self-assembly of membranes formed at the aqueous liquid-liquid interface between supramolecular PA assemblies and polyelectrolytes bearing opposite charges. We used molecular dynamics simulations to understand the importance of interaction strength between the two building blocks as well as building block sizes. With regards to interaction strength, we found two self-assembly regimes predicted by the simulation. We verified these results experimentally by rationally designing a set of supramolecular PAs. The high interaction strength regime, represented by nanofiber-forming PAs with high surface charge density, yields a membrane with a hierarchical structure that includes a robust contact layer and growth of fibrous structures orthogonal to the membrane plane. The

weak interaction strength regime, represented by spherical-aggregated PAs with low surface charge density, yields non-fibrous fingering structures indicative of more typical directional diffusion-aggregation systems. With regards to building block size, we found that chain length of the polymer component can affect membrane structure. Simulations indicate that short chains give thinner initial contact layers, and experiments confirm that the membrane growth after initial contact layer formation is consequently faster with short chains.

## Acknowledgements

This work was supported by the U.S. Department of Energy, Office of Science, Basic Energy Sciences, under Award # DEFG0200ER45810-001. R.H.Z. was supported by an NSF Graduate Research Fellowship. Peptide synthesis was performed in the Peptide Synthesis Core Facility of the Simpson Querrey Institute at Northwestern University. The U.S. Army Research Office, the U.S. Army Medical Research and Materiel Command, and Northwestern University provided funding to develop this facility. Scanning electron microscopy was performed at the NUANCE Center, which receives support from the MRSEC program (NSF DMR-1121262) at the Materials Research Center; the Nanoscale Science and Engineering Center (NSF EEC-0647560) at the International Institute for Nanotechnology; and the State of Illinois, through the International Institute for Nanotechnology. Transmission electron microscopy was performed at the Bioimaging Facility on a JEOL 3200 FETEM purchased with the support of NCRR 1S10RR025092. X-ray scattering studies were performed at the DuPont-Northwestern-Dow Collaborative Access Team (DND-CAT) located at Sector 5 of the Advanced Photon Source (APS). DND-CAT is supported by Northwestern University, E.I. DuPont de Nemours & Co., and The Dow Chemical Company. This research used resources of the Advanced Photon Source, a U.S. Department of Energy (DOE) Office of Science User Facility operated for the DOE Office of Science by Argonne National Laboratory under Contract No. DE-AC02-06CH11357. Circular Dichroism studies were conducted at the Keck Biophysics Facility at Northwestern University. Also, the authors wish to thank the Thaxton Laboratory at Northwestern University for use of the zetasizer. The authors additionally thank Tyson Moyer, Mark McClendon, and Faifan Tantakitti for assistance and discussion regarding PA characterization.

## References

- 1 J. A. A. W. Elemans, A. E. Rowan, R. J. M. Nolte *J. Mater. Chem.*, 2003, **13**, 2661-2670.
- 2 T. Aida, E. W. Meijer, S. I. Stupp, *Science*, 2012, **335**, 813-817.
- 3 H. Cui, T. Muroaka, A. Cheetham, S. I. Stupp, *Nano Lett.*, 2009, **9**, 945-951.
- 4 J. A. Lehrman, H. Cui, W. W. Tsai, T. Moyer, S. I. Stupp, *Chem. Comm.*, 2012, **48**, 9711-9713.
- 5 J. D. Hartgerink, E. Beniash, S. I. Stupp, *Science*, 2001, **294**, 1684-1688.

- 6 J. D. Hartgerink, E. Beniash, S. I. Stupp, *Proc. Natl. Acad. Sci. U. S. A.*, 2002, **99**, 5133-5138.
- 7 E. Beniash, J. D. Hartgerink, H. Storrie, J. C. Stendahl, S. I. Stupp, *Acta Biomater.*, 2005, **1**, 387-397.
- 8 G. Silva, C. Czeisler, K. Niece, E. Beniash, D. Harrington, J. Kessler, and S. I. Stupp, *Science*, 2004, **303**, 1352-1355.
- 9 K. Niece, J. D. Hartgerink, J. J. M. Donners, and S. I. Stupp, *J. Am. Chem. Soc.*, 2003, **125**, 7146-7147.
- 10 J. E. Goldberger, E. J. Berns, R. Bitton, C. J. Newcomb, S. I. Stupp, *Angew. Chem. Int. Ed.*, 2011, **50**, 6292-6295.
- 11 H. Cui, A. G. Cheetham, E. T. Pashuck, S. I. Stupp, *J. Am. Chem. Soc.*, 2014, **136**, 12461-12468.
- 12 T. Muraoka, H. Cui, S. I. Stupp, *J. Am. Chem. Soc.*, 2008, **130**, 2946-2947.
- 13 H. Jiang, M. O. Guler, S. I. Stupp, *Soft Matter*, 2007, **3**, 454-462.
- 14 L. Hsu, G. Cvetanovich, S. I. Stupp, *J. Am. Chem. Soc.*, 2008, **130**, 3892-3899.
- 15 Y. S. Velichko, S. I. Stupp, M. Olvera de la Cruz, *J. Phys. Chem. B.*, 2008, **112**, 2326-2334.
- 16 E. T. Pashuck, S. I. Stupp, *J. Am. Chem. Soc.*, 2010, **132**, 8819-8821.
- 17 S. Zhang, M. A. Greenfield, A. Mata, L. C. Palmer, R. Bitton, J. R. Mantei, C. Aparicio, M. Olvera de la Cruz, S. I. Stupp, *Nature Mater.*, 2010, **9**, 594-601.
- 18 H. Cui, E. T. Pashuck, Y. S. Velichko, S. J. Weigand, A. G. Cheetham, C. J. Newcomb, S. I. Stupp, *Science*, 2010, **327**, 555-559.
- 19 R. Capito, H. Azevedo, Y. S. Velichko, A. Mata, S. I. Stupp, *Science*, 2008, **319**, 1812-1816.
- 20 Y. S. Velichko, J. R. Mantei, R. Bitton, D. Carvajal, K. R. Shull, S. I. Stupp, *Adv. Funct. Mater.*, 2012, **22**, 369-377.
- 21 D. Carvajal, R. Bitton, J. R. Mantei, Y. S. Velichko, S. I. Stupp, K. R. Shull, *Soft Matter*, 2010, **6**, 1816-1823.
- 22 L. W. Chow, R. Bitton, M. J. Webber, D. Carvajal, K. R. Shull, A. K. Sharma, S. I. Stupp, *Biomaterials*, 2011, **32**, 1574-1582.
- 23 R. H. Zha, S. Sur, S. I. Stupp, *Adv. Healthcare Mater.*, 2012, **2**, 126-133.
- 24 R. Bitton, L. W. Chow, R. H. Zha, Y. S. Velichko, E. T. Pashuck, S. I. Stupp, *Small*, 2014, **10**, 500-505.
- 25 T. Kosztolowicz, K. D. Lewandowska, *Phys. Rev. E.*, 2008, **78**, 066103-066114.
- 26 D. Ben-Avraham, S. Havlin, *Diffusion and Reactions in Fractals and Disordered Systems*, Cambridge University Press, Cambridge UK, 2000.
- 27 M. Levitt, *Biochemistry*, 1978, **17**, 4277-4284.
- 28 C. W. A. Kim, J. M. Berg, *Nature*, 1993, **362**, 267-270.
- 29 O. Glatter, O. Kratky, *Small Angle X-ray Scattering*, Academic Press, London, 1982.
- 30 J. H. Ortony, C. J. Newcomb, J. B. Matson, L. C. Palmer, P. E. Doan, B. M. Hoffman, S. I. Stupp, *Nat. Mater.*, 2014, **13**, 812-816.
- 31 K. E. Inostroza-Brito, E. Collin, O. Siton-Mendelson, K. H. Smith, A. Monge-Marcet, D. S. Ferreira, R. P. Rodríguez, M. Alonso, J. C. Rodríguez-Cabello, R. L. Reis, F. Sagués, L. Botto, R. Bitton, H. S. Azevedo, A. Mata, *Nat. Chem.*, 2015, **7**, 897-904.
- 32 T. A. Witten, L. M. Sander, *Phys. Rev. B.*, 1983, **27**, 5686-5697.
- 33 P. Prusinkiewicz, *Artif. Life*, 1993, **1**, 61-74.
- 34 E. L. Cussler, *Diffusion: Mass Transfer in Fluid Systems* (2nd edition), Cambridge University Press, New York, 1997.
- 35 M. Doi, S. F. Edwards, *The Theory of Polymer Dynamics*, Clarendon, Oxford UK, 1989.
- 36 P. G. de Gennes, *Macromol.*, 1976, **9**, 594-598.
- 37 D. Frenkel, B. Smit, *Understanding Molecular Simulation. From Algorithms to Applications*, Academic Press, London, 1996.
- 38 A. Papadopoulou, E. D. Becker, M. Lupkowski, F. van Swol, *J. Chem. Phys.*, 1993, **98**, 4897-4908.
- 39 G. S. Heffelfinger, F. Vanswol, *J. Chem. Phys.*, 1994, **100**, 7548-7552.